Journal of Materials Chemistry C

ROYAL SOCIETY OF CHEMISTRY

PAPER

View Article Online
View Journal | View Issue

Cite this: J. Mater. Chem. C, 2020, 8, 6923

The $In_2SeS/g\text{-}C_3N_4$ heterostructure: a new two-dimensional material for photocatalytic water splitting†

C. He,[a] F. S. Han,[a] J. H. Zhang[a] and W. X. Zhang *[b]

In this work, the structural, electronic and optical properties of the $In_2SeS/g\text{-}C_3N_4$ heterostructure are investigated to explore a highly efficient and spontaneous water splitting photocatalyst by first-principles calculations. The results show that the $In_2SeS/g\text{-}C_3N_4$ heterostructure with a bandgap (E_g) of 2.03 eV is a typical type II semiconductor, which guarantees that the generated electrons and holes can be effectively separated. The potential of the conduction band minimum (CBM) and the valence band maximum (VBM) satisfies the requirements for photocatalytic water splitting. Meanwhile, the $In_2SeS/g\text{-}C_3N_4$ heterostructure has a strong light-absorption ability, and mainly absorbs purple and blue light. In addition, the changes of Gibbs free energy (ΔG) are calculated to understand the oxygen evolution reaction (OER) process of water splitting. Under neutral conditions (pH = 7), the Gibbs free energy continuously decreases during the OER process, verifying the thermodynamic feasibility of water splitting through the $In_2SeS/g\text{-}C_3N_4$ heterostructure. Hence, the $In_2SeS/g\text{-}C_3N_4$ heterostructure is a kind of photocatalyst with excellent performance in the area of photocatalytic water splitting.

Received 19th February 2020, Accepted 9th April 2020

DOI: 10.1039/d0tc00852d

rsc.li/materials-c

Published on 27 dubna 2020. Downloaded on 17.07.2024 0:41:25.

I Introduction

At present, finding new types of pollution-free renewable energy has become a hot topic.[1–4] In recent years, since hydrogen gas has the advantages of stable chemical properties at normal temperature, high combustion heat value and no pollution of the combustion product, it has gained more and more attention and is expected to replace traditional fossil fuels.[5–8] Hydrogen in nature is mainly stored in water in the form of compounds. Therefore, it is an effective way to produce hydrogen gas by photocatalytic water splitting.[9–15] Currently, various types of photocatalysts have been researched extensively, mainly focusing on these two types: oxides represented by TiO_2,[16,17] ZnO[18] and WO_3,[19] and sulfides represented by CdS[20] and ZnS.[21] However, most oxides have the disadvantages of excessively wide bandgap (E_g) and low light-absorption efficiency. Although the sulfides have narrow E_g values, it is easily etched by light during photocatalysis. For example, although CdS has a suitable E_g and band-edge position, the S^{2-} in CdS is more easily oxidized by photogenerated holes than the water molecule, which results in the production of S.[22] Moreover, the electrons and holes of these oxides and sulfides are very easy to recombine. These disadvantages limit the practical applications in the field of photocatalytic water splitting.[23] Therefore, it is necessary to explore a new type of photocatalyst that can absorb sunlight efficiently and separate the electrons and holes easily.

The polymeric graphite-like carbon nitride ($g\text{-}C_3N_4$) is a two-dimensional (2D) layered semiconductor with non-toxicity, chemical stability, low cost and high sensitivity to sunlight.[24–26] Interestingly, $g\text{-}C_3N_4$ has relatively large vacancies and enough adsorption sites.[27,28] Meanwhile, monolayer InM (M = S, Se) has tunable E_g, high sensitivity to sunlight and high carrier mobility compared to most 2D materials.[29,30] Therefore, both $g\text{-}C_3N_4$ and monolayer InM (M = S, Se) have great potential for photocatalytic water splitting. However, the photogenerated electrons and holes of $g\text{-}C_3N_4$ and monolayer InM (M = S, Se) also recombine easily, limiting their application in photocatalytic water splitting. To date, the construction of van der Waals (vdW) heterostructures is considered to be an effective way to modify the atomic and electronic structures of the photocatalysts, which accelerates the separation and transmission of the electrons and holes.[31] For example, $SnSe_2/WSe_2$ vdW heterostructures have been successfully applied to prevent the photogenerated electrons and holes from recombining.[32] Therefore, in this work, we consider designing vdW $In_2SeS/g\text{-}C_3N_4$ heterostructures to effectively prevent the recombination of photogenerated

[a] School of Materials Science and Engineering, Xi'an Jiaotong University, Xi'an 710049, China. E-mail: hecheng@mail.xjtu.edu.cn
[b] School of Materials Science and Engineering, Chang'an University, Xi'an 710064, China. E-mail: wxzhang@chd.edu.cn

† Electronic supplementary information (ESI) available. See DOI: 10.1039/d0tc00852d

electrons and holes and making them retain high sensitivity to sunlight and high carrier mobility.

Herein, first, the most stable structure of the $In_2SeS/g\text{-}C_3N_4$ heterostructure is found through geometric optimization. Then, we have analyzed the electronic and optical properties of the $In_2SeS/g\text{-}C_3N_4$ heterostructure, and found that it is a typical type II semiconductor, and mainly absorbs blue and purple light. Furthermore, in order to investigate the thermodynamic feasibility of photocatalytic water splitting, the changes in Gibbs free energy (ΔG) are calculated during the oxygen evolution reaction (OER) that occurred on the $g\text{-}C_3N_4$ layer side. The results show that the $In_2SeS/g\text{-}C_3N_4$ heterostructure is a kind of photocatalyst with excellent performance in the area of photocatalytic water splitting.

Published on 27 dubna 2020. Downloaded on 17.07.2024 0:41:25.

II Theoretical approach

The first-principles calculations were performed by the Vienna Ab initio Simulation Package (VASP) with the projector augmented wave (PAW), based on density functional theory (DFT).[33,34] The generalized gradient approximation (GGA) and Perdew–Burke–Ernzerh (PBE) were adopted to treat the exchange–correlation interaction of electrons.[35,36] Because of the underestimation of the PBE functional on the band gap of the semiconductor, the HSE06[37] hybrid functional was applied for calculations of more accurate electronic properties. Meanwhile, the GW[38,39] approximation combined with the Bethe–Salpeter equation (BSE)[40] was employed to predict the optical properties. In addition, considering the vdW interactions between the layers, the empirical correction scheme of the DFT-D3 (D stands for dispersion) approach within the Grimme scheme was adopted.[41] A vacuum spacing of 25 Å was added along the direction perpendicular to 2D nanosheets to avoid the interlayer interactions caused by periodicity. A Monkhorst–Pack k-point mesh of $7 \times 7 \times 1$ was used to calculate the properties of all studied samples in the 2D Brillouin zone. The cut-off energy was set to 600 eV. The convergence tolerances for energy, maximum force and displacement on each atom during structural relaxation were set to 10^{-5} eV, 0.03 eV $Å^{-1}$ and 0.003 Å, respectively.

III Results and discussion

3.1 Structures and stabilities of $In_2SeS/g\text{-}C_3N_4$

The calculated lattice parameters of $g\text{-}C_3N_4$ ($a = b = 7.06$ Å) and monolayer In_2SeS ($a = b = 3.95$ Å) are in good agreement with the other theoretical calculations and experimental result.[42,43] Meanwhile, the phonon spectrum of monolayer In_2SeS is shown in Fig. S1 (ESI†). There is no virtual frequency in the phonon spectrum, which proves that the optimized structure of monolayer In_2SeS is stable. The $In_2SeS/g\text{-}C_3N_4$ vdW heterostructure is achieved by a 1×1 $g\text{-}C_3N_4$ supercell and a $\sqrt{3} \times \sqrt{3}$ monolayer In_2SeS supercell stacked in the vertical direction with a lattice mismatch of about 3%. According to the different stacking patterns of $g\text{-}C_3N_4$ and monolayer In_2SeS, twelve

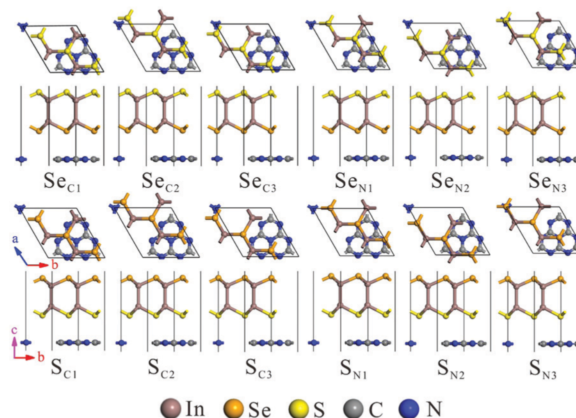

Fig. 1 Top and side views of the $In_2SeS/g\text{-}C_3N_4$ heterostructure at different stacking patterns: Se_{C1}, Se_{C2}, Se_{C3}, Se_{N1}, Se_{N2}, Se_{N3}, S_{C1}, S_{C2}, S_{C3}, S_{N1}, S_{N2} and S_{N3}.

different heterostructures are constructed, as shown in Fig. 1. When Se atoms are adjacent to the $g\text{-}C_3N_4$ layer and C or N atoms are located in the hexagonal ring center of the In_2SeS layer, the heterostructures are labeled as Se_{C1}, Se_{C2}, Se_{C3}, Se_{N1}, Se_{N2} and Se_{N3}. When S atoms are adjacent to the $g\text{-}C_3N_4$ layer and C or N atoms are located in the hexagonal ring center of the In_2SeS layer, the heterostructures are labeled as S_{C1}, S_{C2}, S_{C3}, S_{N1}, S_{N2} and S_{N3}. To check the stability of the structure, the binding energy (E_b) of the 12 heterostructures are calculated using the following formula:[44]

$$E_b = E_{g\text{-}C_3N_4/In_2SeS} - E_{g\text{-}C_3N_4} - E_{In_2SeS} \quad (1)$$

where $E_{g\text{-}C_3N_4/In_2SeS}$, $E_{g\text{-}C_3N_4}$ and E_{In_2SeS} represent the total energy of the $In_2Se/g\text{-}C_3N_4$ heterostructure, $g\text{-}C_3N_4$ and monolayer In_2SeS, respectively. According to the definition, a negative value of E_b indicates that the heterostructure system is energetically stable. Meanwhile, the more negative the value of E_b is, the more stable the heterostructure is. Therefore, as shown in Table 1, the smallest E_b (−2.21 eV) of the S_{N1} stacking pattern means that it is the most stable among the twelve stacking patterns. Moreover, to find the most suitable interlayer distance (d_0) of the S_{N1} stacking pattern, E_b of the S_{N1} stacking pattern is calculated as a function of d_0, which is shown in Fig. S2 (ESI†). When d_0 = 3 Å, E_b is −2.29 eV, and it is the most negative value among them. Thus the S_{N1} stacking pattern with a d_0 of 3 Å is the most stable. As shown in Table S1 (ESI†), the convergence

Table 1 Interlayer spacing and binding energy of the $In_2Se/g\text{-}C_3N_4$ heterostructure

Type	$In_2SeS/g\text{-}C_3N_4$					
Stacking patterns	Se_{C1}	Se_{C2}	Se_{C3}	Se_{N1}	Se_{N2}	Se_{N3}
E_b (eV)	−2.161	−1.422	−2.044	−1.295	−1.505	−1.520
d_0 (Å)	2.872	2.847	2.830	3.142	3.134	2.667
Stacking patterns	S_{C1}	S_{C2}	S_{C3}	S_{N1}	S_{N2}	S_{N3}
E_b (eV)	−2.128	−2.108	−2.092	−2.210	−1.462	−1.948
d_0 (Å)	2.731	2.783	2.781	2.848	3.041	3.042

This journal is © The Royal Society of Chemistry 2020

Published on 27 dubna 2020. Downloaded on 17.07.2024 0:41:25.

test results also show that the S_{N1} stacking pattern is stable, so it is chosen for further calculation.

3.2 Electronic properties of $In_2SeS/g\text{-}C_3N_4$

In order to investigate the electronic properties of the $In_2SeS/g\text{-}C_3N_4$ heterostructure, the charge distribution and charge transfer are considered by analyzing the planar average charge density ($\rho(z)$) and the planar average charge density difference ($\Delta\rho(z)$). $\Delta\rho(z)$ is given by the following formula:[45]

$$\Delta\rho(z) = \rho(z)_{In_2SeS/g\text{-}C_3N_4} - \rho(z)_{g\text{-}C_3N_4} - \rho(z)_{In_2SeS} \quad (2)$$

where $\rho(z)_{In_2SeS/g\text{-}C_3N_4}$, $\rho(z)_{g\text{-}C_3N_4}$ and $\rho(z)_{In_2SeS}$ are $\rho(z)$ of the $In_2SeS/g\text{-}C_3N_4$ heterostructure, $g\text{-}C_3N_4$ and monolayer In_2SeS, respectively. In Fig. S3 (ESI†), $\rho(z)$ values of $g\text{-}C_3N_4$, monolayer In_2SeS and the $In_2SeS/g\text{-}C_3N_4$ heterostructure are given. In Fig. 2, we can see that charges accumulate in the In_2SeS layer and dissipates in the $g\text{-}C_3N_4$ layer, indicating that electrons are transferred from the $g\text{-}C_3N_4$ layer to the In_2SeS layer. Thus the electrons and holes are effectively separated, which is conducive to the water splitting of the $In_2SeS/g\text{-}C_3N_4$ heterostructure. To further study the interfacial electronic properties, the interface dipole moment $\mu(z)$ is also calculated using the following formula:[45]

$$\mu(z) = \int z\Delta\rho(z)\mathrm{d}z \quad (3)$$

A $\mu(z)$ of -0.23 D from the $g\text{-}C_3N_4$ layer to the In_2SeS layer is found by calculation, confirming the formation of a heterostructure-induced interface dipole.

Moreover, the energy bands of $g\text{-}C_3N_4$, monolayer In_2SeS and the $In_2SeS/g\text{-}C_3N_4$ heterostructure are calculated, as shown in Fig. 3. Both $g\text{-}C_3N_4$ and monolayer In_2SeS are indirect bandgap semiconductors with E_g values of 2.67 eV and 2.33 eV at the HSE06 level, respectively. Surprisingly, the $In_2SeS/g\text{-}C_3N_4$ heterostructure is a direct bandgap semiconductor with an E_g of 2.03 eV, which is in the energy range of visible light (1.6–3.2 eV). Meanwhile, the top band of the valence band is mainly contributed by the $g\text{-}C_3N_4$ layer and the bottom band of the conduction band is mainly contributed by the In_2SeS layer, which indicates that the

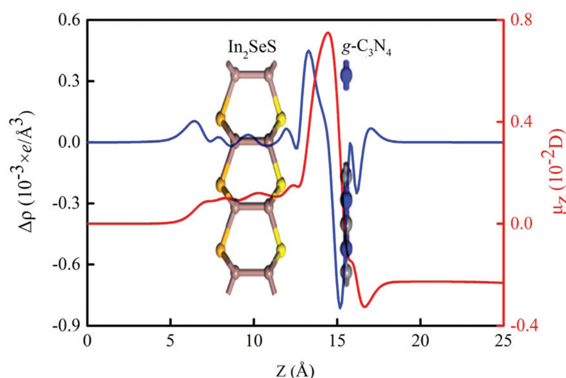

Fig. 2 Planar average charge density difference (blue line) and interfacial dipole moment (red line) along the Z-direction for the $In_2SeS/g\text{-}C_3N_4$ heterostructure.

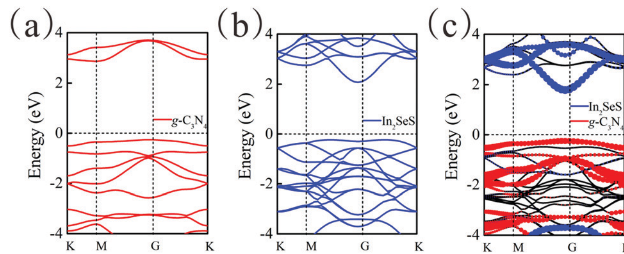

Fig. 3 (a) Band structure of $g\text{-}C_3N_4$. (b) Band structure of monolayer In_2SeS. (c) Band structure of the $In_2SeS/g\text{-}C_3N_4$ heterostructure.

electrons and holes are separated after the formation of the heterostructure and the $In_2SeS/g\text{-}C_3N_4$ heterostructure is a type-II heterostructure. Meanwhile, the total density of states (TDOS) and the projected density of states (PDOS) for the $In_2SeS/g\text{-}C_3N_4$ heterostructure are calculated. As shown in Fig. 4, the peak with the highest energy below the Fermi level is basically provided by the N–p orbit while the peak with the lowest energy above the Fermi level is basically provided by the In–s orbit, which implies that the positions of N and In atoms are better adsorption sites and also illustrates the separation of electrons and holes.

Furthermore, the carrier mobility (μ) of the $In_2SeS/g\text{-}C_3N_4$ heterostructure is also calculated using the formula[46–49]

$$\mu_{2D} = \frac{e^3 C_{2D}}{k_b T (m^*)^2 (E_1^i)^2} \quad (4)$$

where e is the electron charge, $\hbar$ is Planck's constant divided by 2π and k_b is Boltzmann's constant. T is the temperature, which is set to 298.15 K in our calculation to simulate room temperature. m^* is the effective mass of an electron or hole, which is calculated using the formula

$$\frac{1}{m^*} = \frac{1}{\hbar^2}\frac{\partial^2 E(k)}{k^2} \quad (5)$$

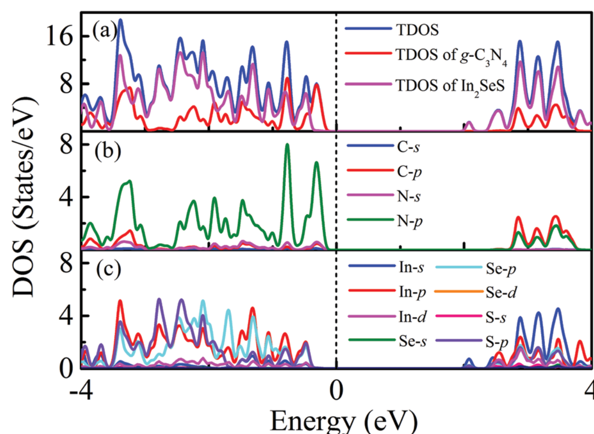

Fig. 4 (a) TDOS of the $In_2SeS/g\text{-}C_3N_4$ heterostructure, PDOS of the $g\text{-}C_3N_4$ layer in the $In_2SeS/g\text{-}C_3N_4$ heterostructure and PDOS of the In_2SeS layer in the $In_2SeS/g\text{-}C_3N_4$ heterostructure. (b) PDOS of C and N atoms in the $g\text{-}C_3N_4$ layer. (c) PDOS of In, Se and S atoms in the In_2SeS layer.

View Article Online

Published on 27 dubna 2020. Downloaded on 17.07.2024 0:41:25.

where E is the total energy and k is the wave vector. Then, C_{2D} is the 2D elastic modulus, which is calculated using the formula

$$\frac{E - E_0}{S_0} = C_{2D}\frac{(\Delta l/l_0)^2}{2} \tag{6}$$

where E and E_0 are the total energy of the crystal with and without deformation and S_0 is the lattice volume of the equilibrium state. Δl and l_0 are the variation of the lattice length and the initial lattice length, respectively. Then, E_l^i is the deformation potential constant of the valence band maximum (VBM) for holes or the conduction band minimum (CBM) for electrons along the transport direction, which is calculated using the formula

$$E_l^i = \frac{\Delta V_i}{\Delta l/l_0} \tag{7}$$

where ΔV_i is the energy change of the ith band under compression and tension. According to the above formula, the effective mass of the electrons and holes are $0.114m_0$ and $1.36m_0$, respectively. Energy changes of the $In_2SeS/g\text{-}C_3N_4$ heterostructure with strains in the X-direction and the Y-direction are given, as shown in Fig. S4 (ESI†). C_{2D} values are both 87.89 J m^{-2} along the X-direction and the Y-direction by calculation, and the electron and hole mobilities are 1665 $cm^2\ V^{-1}\ s^{-1}$ and 12 $cm^2\ V^{-1}\ s^{-1}$, respectively. The electron mobility is a relatively large value compared to other 2D materials, which is conducive to photocatalytic water splitting. Meanwhile, we have calculated the effective mass and carrier mobility of the $In_2SeS/g\text{-}C_3N_4$ heterostructure with a strain (from −3% to 3%) applied in the X-direction and the Y-direction, respectively, as shown in Table S2 (ESI†). It is found that the strain has little effect on the carrier mobility of the $In_2SeS/g\text{-}C_3N_4$ heterostructure.

Then, the electrostatic potentials of $g\text{-}C_3N_4$, monolayer In_2SeS and the $In_2SeS/g\text{-}C_3N_4$ heterostructure are calculated. Moreover, their work function (φ) is also calculated, which is given by the formula

$$\varphi = E_{vac} - E_f \tag{8}$$

where E_{vac} is the electrostatic potential in a vacuum near to the surface. E_f is the electrostatic potential at the Fermi level. As shown in Fig. 5, φ values of $g\text{-}C_3N_4$, monolayer In_2SeS and the $In_2SeS/g\text{-}C_3N_4$ heterostructure are 5.38 eV, 6.19 eV and 5.93 eV, respectively, which means that the $g\text{-}C_3N_4$ layer is easier to lose electrons than the In_2SeS layer. Moreover, the standard oxidation potential of O_2/H_2O can be calculated using $E_{O_2/H_2O} = -5.67$ eV + pH × 0.059 eV and the standard hydrogen potential of H^+/H_2 can be calculated using $E_{H^+/H_2} = -4.44$ eV + pH × 0.059 eV.[50,51] To satisfy the requirements for photocatalytic water splitting, the potential of the CBM for photocatalysts should be higher than the standard hydrogen potential and the potential of the VBM for photocatalysts should be lower than the standard oxygen potential.[52] Therefore, based on the value of φ, we have obtained the potentials at the Fermi level for $g\text{-}C_3N_4$, monolayer In_2SeS and the $In_2SeS/g\text{-}C_3N_4$ heterostructure. Their values are −5.38 eV, −6.19 eV and −5.93 eV, respectively. Then, based on the relative positions of the CBM, the VBM and the Fermi level (obtained according to Fig. 3), we have calculated the potentials of band-edge positions for $g\text{-}C_3N_4$, monolayer In_2SeS and the $In_2SeS/g\text{-}C_3N_4$ heterostructure, as shown in Fig. 6. The values of potential at CBM and at VBM for $g\text{-}C_3N_4$ are −3.25 eV and −5.92 eV,

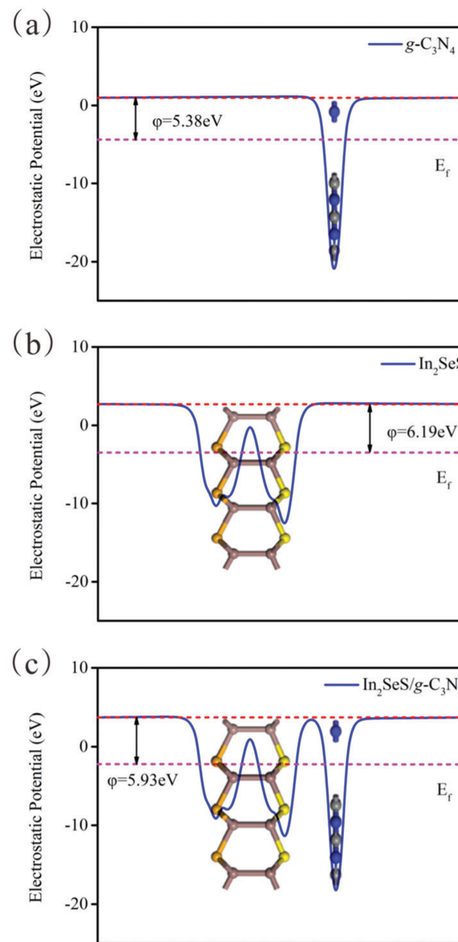

Fig. 5 (a) Electrostatic potential of $g\text{-}C_3N_4$. (b) Electrostatic potential of monolayer In_2SeS. (c) Electrostatic potential of the $In_2SeS/g\text{-}C_3N_4$ heterostructure. The red and pink dashed lines denote the Fermi level and the vacuum energy level, respectively.

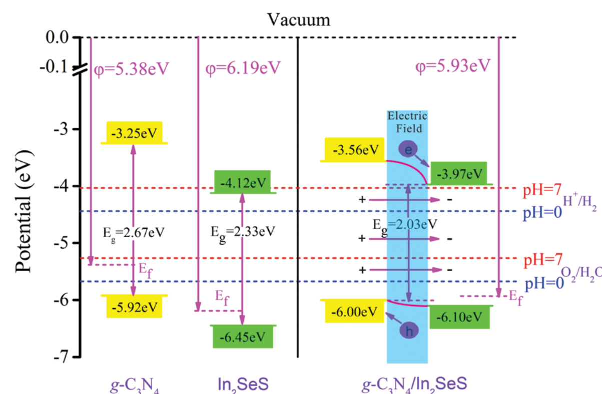

Fig. 6 Potential of band-edge positions for $g\text{-}C_3N_4$, monolayer In_2SeS and the $In_2SeS/g\text{-}C_3N_4$ heterostructure.

This journal is © The Royal Society of Chemistry 2020

View Article Online

Published on 27 dubna 2020. Downloaded on 17.07.2024 0:41:25.

respectively. The values of potential at the CBM and at the VBM for monolayer In_2SeS are −4.12 eV and −6.45 eV, respectively. After the heterostructure is formed, the value of the potential at the CBM for the In_2SeS/g-C_3N_4 heterostructure is 3.97 eV, which is higher than the standard hydrogen potential (4.44 eV at pH = 0 and 4.01 eV at pH = 7). In addition, the value of the potential at the VBM for the In_2SeS/g-C_3N_4 heterostructure is 6.00 eV, which is lower than the standard oxygen potential (5.67 eV at pH = 0 and 5.26 eV at pH = 7). Therefore, in terms of potential, the In_2SeS/g-C_3N_4 heterostructure meets the requirements for photocatalytic water splitting. Part electrons are transferred from the g-C_3N_4 layer to the In_2SeS layer, which leads to the formation of an internal electric field from the g-C_3N_4 layer to the In_2SeS layer. The g-C_3N_4 layer is similar to the anode when electrolyzing water and the oxygen evolution reaction (OER) occurs. The In_2SeS layer is similar to the cathode of electrolyzing water and the hydrogen evolution reaction (HER) occurs.

Besides, the In_2SeS/g-C_3N_4 heterostructure is applied with biaxial strain. We find that the In_2SeS/g-C_3N_4 heterostructure can withstand the biaxial strain from −6% to +6% without damaging its structure. As shown in Fig. 7, when the values of biaxial strain are −6%, −4%, −2%, 2%, 4% and 6%, the E_g values of the In_2SeS/g-C_3N_4 heterostructure are 3.16 eV, 3.01 eV, 2.64 eV, 1.83 eV, 1.51 eV and 1.19 eV, respectively. It is concluded that E_g increases with the decrease of biaxial strain and E_g decreases with the increase of biaxial strain. Among them, when the value of biaxial strain is 2%, the In_2SeS/g-C_3N_4 heterostructure is still a direct bandgap semiconductor. When the tensile stress is greater than 2% or compressive stress is applied, the In_2SeS/g-C_3N_4 heterostructure will have a transition from a direct bandgap semiconductor to an indirect bandgap semiconductor. The potentials of band-edge positions under different biaxial strain conditions are shown in Fig. 8. When −6%, −4%, −2% and 2% biaxial strains are applied, the potentials of the VBM and the CBM still satisfy the requirements for photocatalytic water splitting. When 4% and 6% biaxial strains are applied, the potentials of the VBM and the CBM cannot satisfy the requirements for photocatalytic water splitting. It is noted that the larger the E_g of the heterostructure is, the greater the driving force for photocatalytic water splitting is. However, once E_g is too large, the energy required for electronic transition from the valence band to the conduction band increases and the wavelength range of sunlight that can provide sufficient energy reduces, which is not conducive to photocatalytic water splitting. Therefore, when −2% biaxial strain is applied, the effect of the In_2SeS/g-C_3N_4 heterostructure for photocatalytic water splitting is the best in theory.

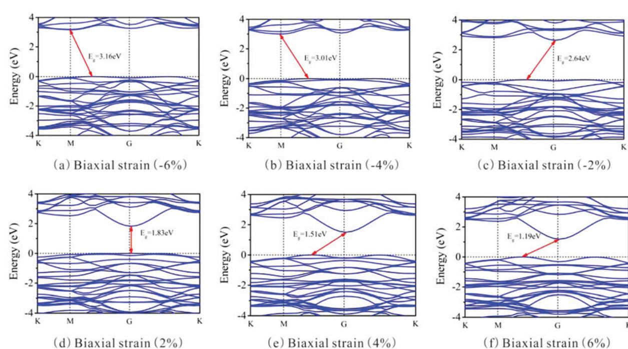

Fig. 7 Band structure under different biaxial strain conditions.

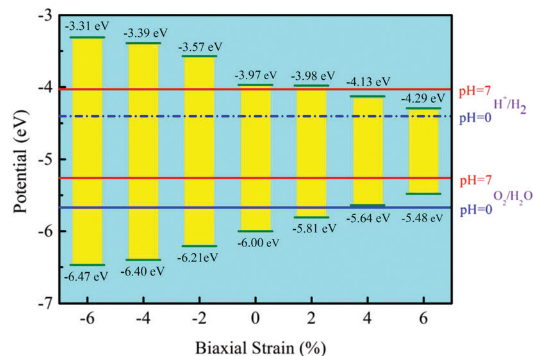

Fig. 8 Potential of band-edge positions under different biaxial strain conditions.

3.3 Optical properties of In_2SeS/g-C_3N_4

In addition, the optical properties of the In_2SeS/g-C_3N_4 heterostructure are predicted by using the GW+BSE approach. The real part (ε_1) and the imaginary part (ε_2) describe the dielectric properties and light-absorption ability of the material, respectively. The imaginary part (ε_2) can be determined using the formula[53–55]

$$\varepsilon_2(\omega) = \frac{2e^2\pi}{\Omega\varepsilon_0}\sum_{k,c,\nu}\left|\left\{\psi_k^c|\mu\cdot r|\psi_k^\nu\right\}\right|^2\delta\left(E_k^c - E_k^\nu - E\right) \tag{9}$$

where ω represents the frequency of the electromagnetic radiation in energy units. Ω and ε_0 represent the cell volume and the dielectric constant in free space, respectively. c and ν represent the conduction and valence band states, respectively. u and r represent the vector defining the polarization of the incident electric field and the position vector, respectively. As shown in Fig. 9, the light-absorption ability of the In_2SeS/g-C_3N_4

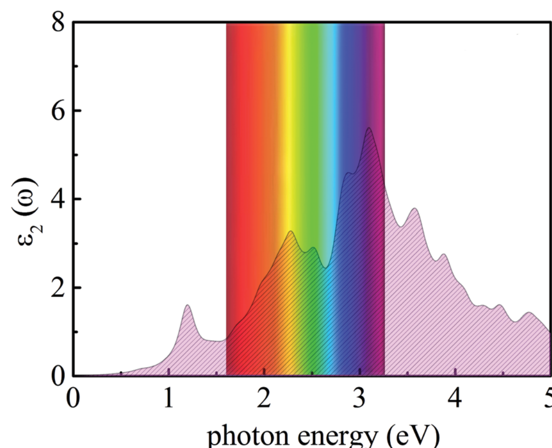

Fig. 9 Absorption spectrum of light.

heterostructure is relatively strong. The highest light-absorption peak is between blue and purple light (corresponding to a photon energy of about 3 eV, and E_g of the $In_2SeS/g\text{-}C_3N_4$ heterostructure is 2.03 eV), which indicates that after the $In_2SeS/g\text{-}C_3N_4$ heterostructure absorbs the photons, there is enough energy to promote the electron to transit from the valence band to the conduction band.

3.4 Thermodynamic feasibility of the $In_2SeS/g\text{-}C_3N_4$ heterostructure for photocatalytic water splitting

Finally, we have explored the thermodynamic feasibility of the $In_2SeS/g\text{-}C_3N_4$ heterostructure for photocatalytic water splitting. The reaction of water splitting can be divided into two half reactions: the HER in the cathode and the OER in the anode. The reaction step of the HER is:[28]

$$2H^+ + 2e^- \rightarrow H_2 \quad (10)$$

and the OER is divided into 4 small steps:[56,57]

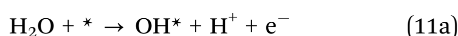

$$H_2O + * \rightarrow OH* + H^+ + e^- \quad (11a)$$

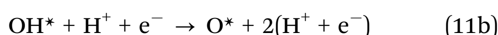

$$OH* + H^+ + e^- \rightarrow O* + 2(H^+ + e^-) \quad (11b)$$

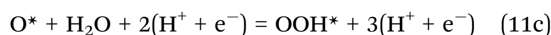

$$O* + H_2O + 2(H^+ + e^-) = OOH* + 3(H^+ + e^-) \quad (11c)$$

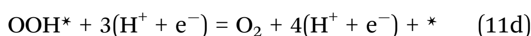

$$OOH* + 3(H^+ + e^-) = O_2 + 4(H^+ + e^-) + * \quad (11d)$$

where * indicates the $In_2SeS/g\text{-}C_3N_4$ heterostructure substrate. OH*, O* and OOH* indicate that OH, O and OOH are adsorbed on the substrate, respectively. ΔG is calculated using the formula[58,59]

$$\Delta G = \Delta E + \Delta ZPE - T\Delta S - \Delta G_U - \Delta G_{pH} \quad (12)$$

where ΔE represents the change in total energy. ΔZPE represents the change in zero point energy. ZPE could be calculated by

$$ZPE = 1/2\sum h\nu \quad (13)$$

where ν represents the vibrational frequency. Then, $T\Delta S$ represents the change in entropic contributions (T is set to be 298.15 K). TS could be calculated by

$$TS = k_b T\left[\sum_K \ln\left(\frac{1}{1 - e^{-h\nu/k_b T}}\right) + \sum_K \frac{h\nu}{k_b T}\left(\frac{1}{e^{h\nu/k_b T} - 1}\right) + 1\right] \quad (14)$$

where e represents the electron charge, h represents Planck's constant and k_b is Boltzmann's constant. Then, ΔG_U represents the effect of electrochemical potential on ΔG, which is calculated by:

$$\Delta G_U = -eU \quad (15)$$

where U represents the potential difference from the standard hydrogen electrode potential. Then, ΔG_{pH} represents the effect of the pH value on ΔG, which is calculated by:

$$\Delta G_{pH} = -k_b T \ln 10 \times pH \quad (16)$$

Here, pH = 0 and pH = 7 are considered. Theoretically, the HER is relatively easy under the action of the potential and thus we only need to consider the feasibility of the OER in thermodynamics. Fig. 10(a)–(c) show the most stable adsorption site of OH, O and OOH on the $g\text{-}C_3N_4$ side of the $In_2SeS/g\text{-}C_3N_4$ heterostructure, respectively. In Fig. 10(d), when pH = 0, U = 0 V, ΔG increases every step to 4.55 eV eventually. When pH = 0 and U = 1.23 V (minimum potential difference required for water splitting), ΔG declines in the first and third reactions while it increases in the second and fourth reactions. The actual electrochemical driving force of the OER is 1.56 eV at pH = 0 (potential difference between the potential of the VBM and the standard hydrogen potential). When pH = 0 and U = 1.56 V, ΔG declines in

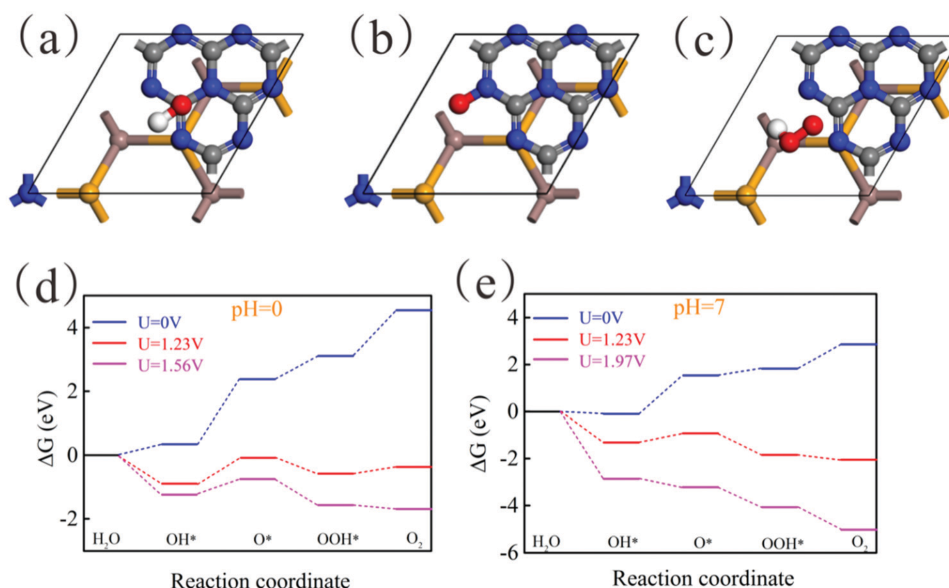

Fig. 10 (a)–(c) Optimized geometries of OH, O and OOH on the $In_2SeS/g\text{-}C_3N_4$ heterostructure during OER. (d) The changes of Gibbs free energy at pH = 0 and at different potential differences (0 V, 1.23 V and 1.56 V). (e) The changes of Gibbs free energy at pH = 7 and at different potential differences (0 V, 1.23 V and 1.97 V).

Published on 27 dubna 2020. Downloaded on 17.07.2024 0:41:25.

This journal is © The Royal Society of Chemistry 2020

Published on 27 dubna 2020. Downloaded on 17.07.2024 0:41:25.

the first, third and fourth reactions while it increases in the second reaction. In all, when pH = 0, the existence of the increase of ΔG leads to the failure of water splitting for the $In_2SeS/g\text{-}C_3N_4$ heterostructure in thermodynamics. In Fig. 10(e), when pH = 7 and U = 0 V, ΔG increases every step to 2.86 eV eventually. When pH = 7 and U = 1.23 V, ΔG declines in the first, third and fourth reactions while it increases in the second reaction. Therefore, when pH = 7, U = 0 or 1.23 eV, it is also impossible to split water for the $In_2SeS/g\text{-}C_3N_4$ heterostructure in thermodynamics. The actual electrochemical driving force of the OER is 1.56 eV at pH = 7. When pH = 7 and U = 1.97 V, ΔG declines every step of the OER, which indicates that the $In_2SeS/g\text{-}C_3N_4$ heterostructure for photocatalytic water splitting becomes feasible in thermodynamics under this condition.

IV Conclusions

Twelve structures of the $In_2SeS/g\text{-}C_3N_4$ heterostructures are constructed according to different stacking patterns. Through the first-principles calculations, we find that the S_{N1} stacking pattern of the $In_2SeS/g\text{-}C_3N_4$ heterostructure with a d_0 of 3 Å is the most stable, and the $In_2SeS/g\text{-}C_3N_4$ heterostructure is a typical type-II semiconductor with a direct bandgap of 2.03 eV, whose CBM and VBM are contributed by the In_2SeS layer and the $g\text{-}C_3N_4$ layer, respectively. The potentials at the CBM and the VBM satisfy the requirements for photocatalytic water splitting. The electron mobility is 1665 $cm^2\ V^{-1}\ s^{-1}$, which is a relatively large value compared to other 2D materials. Meanwhile, the $In_2SeS/g\text{-}C_3N_4$ heterostructure has a strong ability to absorb light, mainly absorbing blue and purple light. In addition, when pH = 7 and U = 1.97 V, ΔG goes down every step of the OER, which verifies the feasibility of photocatalytic water splitting in thermodynamics. In short, the $In_2SeS/g\text{-}C_3N_4$ heterostructure is expected to be a good candidate for photocatalytic water splitting.

Conflicts of interest

There are no conflicts to declare.

Acknowledgements

The authors acknowledge the support from the National Natural Science Foundation of China (NSFC, Grant No. 51471124, U1766216), the National Key R&D Program of China (2018YFB0905600) and the Natural Science Foundation of Shaanxi Province, China (2019JM-189, 2020JM-218).

Notes and references

1 J. W. Ager and A. A. Lapkin, *Science*, 2018, **360**, 707–708.
2 X. J. Huang, Q. B. Meng, H. Chen, X. L. Du and L. Q. Chen, *Science*, 2018, **360**, 47–51.
3 Y. Zhou and Y. S. Liu, *Nature*, 2018, **560**, 29.
4 S. G. Anton and A. E. A. Nucu, *Renewable Energy*, 2020, **147**, 330–338.
5 F. Gutierrez-Martin, A. B. Calcerrada, A. de Lucas-Consuegra and F. Dorado, *Renewable Energy*, 2020, **147**, 639–649.
6 H. Mehrjerdi, A. Iqbal, E. Rakhshani and J. R. Torres, *Energy Convers. Manage.*, 2019, **201**, 11.
7 H. Ishaq and I. Dincer, *J. Cleaner Prod.*, 2020, **246**, 12.
8 C. J. Quarton, O. Tlili, L. Welder, C. Mansilla, H. Blanco, H. Heinrichs, J. Leaver, N. J. Samsatli, P. Lucchese, M. Robinius and S. Samsatli, *Sustainable Energy Fuels*, 2020, **4**, 80–95.
9 M. Chauhan, K. Soni, P. E. Karthik, K. P. Reddy, C. S. Gopinath and S. Deka, *J. Mater. Chem. A*, 2019, **7**, 6985–6994.
10 Y. J. Wu, C. B. Cao, C. Qiao, Y. Wu, L. F. Yang and W. Younas, *J. Mater. Chem. C*, 2019, **7**, 10613–10622.
11 J. Z. Liu, Y. H. Li, X. D. Zhou, H. Jiang, H. G. Yang and C. Z. Li, *J. Mater. Chem. A*, 2020, **8**, 17–26.
12 J. Zhu, M. Sun, S. J. Liu, X. H. Liu, K. Hu and L. Wang, *J. Mater. Chem. A*, 2019, **7**, 26975–26983.
13 K. Maeda, K. Teramura, D. L. Lu, T. Takata, N. Saito, Y. Inoue and K. Domen, *Nature*, 2006, **440**, 295.
14 F. F. Hu, L. Q. Tao, H. Y. Ye, X. D. Li and X. P. Chen, *J. Mater. Chem. C*, 2019, **7**, 7104–7113.
15 T. Hisatomi, J. Kubota and K. Domen, *Chem. Soc. Rev.*, 2014, **43**, 7520–7535.
16 S. Cao, T. S. Chan, Y. R. Lu, X. H. Shi, B. Fu, Z. J. Wu, H. M. Li, K. Liu, S. Alzuabi, P. Cheng, M. Liu, T. Li, X. B. Chen and L. Y. Piao, *Nano Energy*, 2020, **67**, 9.
17 Y. Li, Q. Q. Shen, R. F. Guan, J. B. Xue, X. G. Liu, H. S. Jia, B. S. Xu and Y. C. Wu, *J. Mater. Chem. C*, 2020, **8**, 1025–1040.
18 V. Etacheri, R. Roshan and V. Kumar, *ACS Appl. Mater. Interfaces*, 2012, **4**, 2717–2725.
19 I. M. Szilagyi, B. Forizs, O. Rosseler, A. Szegedi, P. Nemeth, P. Kiraly, G. Tarkanyi, B. Vajna, K. Varga-Josepovits, K. Laszlo, A. L. Toth, P. Baranyai and M. Leskela, *J. Catal.*, 2012, **294**, 119–127.
20 X. F. Ning and G. X. Lu, *Nanoscale*, 2020, **12**, 1213–1223.
21 A. R. Amani-Ghadim, F. Khodam and M. S. S. Dorraji, *J. Mater. Chem. A*, 2019, **7**, 11408–11422.
22 A. Kudo and Y. Miseki, *Chem. Soc. Rev.*, 2009, **38**, 253–278.
23 H. Y. Liu, C. L. Yang, M. S. Wang and X. G. Ma, *Appl. Surf. Sci.*, 2020, **501**, 7.
24 J. Q. Wen, J. Xie, X. B. Chen and X. Li, *Appl. Surf. Sci.*, 2017, **391**, 72–123.
25 S. W. Cao and J. G. Yu, *J. Phys. Chem. Lett.*, 2014, **5**, 2101–2107.
26 X. Y. Du, X. Bai, L. Xu, L. Yang and P. K. Jin, *Chem. Eng. J.*, 2020, **384**, 14.
27 Y. H. Li, M. L. Gu, T. Shi, W. Cui, X. M. Zhang, F. Dong, J. S. Cheng, J. J. Fan and K. L. Lv, *Appl. Catal., B*, 2020, **262**, 11.
28 S. Lin, X. X. Ye, X. M. Gao and J. Huang, *J. Mol. Catal. A: Chem.*, 2015, **406**, 137–144.
29 A. V. Bandura, D. D. Kuruch and R. A. Evarestov, *Isr. J. Chem.*, 2017, **57**, 490–500.
30 M. Isik and N. M. Gasanly, *Mater. Sci. Semicond. Process.*, 2020, **107**, 5.

View Article Online

Published on 27 dubna 2020. Downloaded on 17.07.2024 0:41:25.

31 R. Q. Zhang, L. L. Zhang, Q. J. Zheng, P. F. Gao, J. Zhao and J. L. Yang, *J. Phys. Chem. Lett.*, 2018, **9**, 5419–5424.
32 X. Yan, C. S. Liu, C. Li, W. Z. Bao, S. J. Ding, D. W. Zhang and P. Zhou, *Small*, 2017, **13**, 8.
33 L. J. Sham and W. Kohn, *Phys. Rev.*, 1966, **145**, 561–567.
34 G. Kresse and J. Furthmuller, *Phys. Rev. B: Condens. Matter Mater. Phys.*, 1996, **54**, 11169–11186.
35 G. R. Su, S. Yang, S. Li, C. J. Butch, S. N. Filimonov, J. C. Ren and W. Liu, *J. Am. Chem. Soc.*, 2019, **141**, 1628–1635.
36 J. P. Perdew, K. Burke and M. Ernzerhof, *Phys. Rev. Lett.*, 1996, **77**, 3865–3868.
37 J. Heyd, G. E. Scuseria and M. Ernzerhof, *J. Chem. Phys.*, 2003, **118**, 8207–8215.
38 P. Umari, G. Stenuit and S. Baroni, *Phys. Rev. B: Condens. Matter Mater. Phys.*, 2009, **79**, 4.
39 P. Umari, G. Stenuit and S. Baroni, *Phys. Rev. B: Condens. Matter Mater. Phys.*, 2010, **81**, 5.
40 E. E. Salpeter and H. A. Bethe, *Phys. Rev.*, 1951, **84**, 1232–1242.
41 S. Grimme, *J. Comput. Chem.*, 2006, **27**, 1787–1799.
42 M. M. Dong, C. He and W. X. Zhang, *J. Mater. Chem. C*, 2017, **5**, 3830–3837.
43 M. Ganaie and M. Zulfequar, *J. Alloys Compd.*, 2016, **687**, 643–651.
44 C. He, J. H. Zhang, W. X. Zhang and T. T. Li, *J. Phys. Chem. C*, 2019, **123**, 5157–5163.
45 C. He, J. H. Zhang, W. X. Zhang and T. T. Li, *J. Phys. Chem. Lett.*, 2019, **10**, 3122–3128.
46 S. Bruzzone and G. Fiori, *Appl. Phys. Lett.*, 2011, **99**, 3.
47 S. Takagi, A. Toriumi, M. Iwase and H. Tango, *IEEE Trans. Electron Devices*, 1994, **41**, 2357–2362.
48 G. Fiori and G. Iannaccone, *Proc. IEEE*, 2013, **101**, 1653–1669.
49 J. S. Qiao, X. H. Kong, Z. X. Hu, F. Yang and W. Ji, *Nat. Commun.*, 2014, **5**, 7.
50 H. L. L. Zhuang and R. G. Hennig, *Chem. Mater.*, 2013, **25**, 3232–3238.
51 H. C. Yang, J. J. Li, L. Yu, B. B. Huang, Y. D. Ma and Y. Dai, *J. Mater. Chem. A*, 2018, **6**, 4161–4166.
52 R. M. N. Yerga, M. C. A. Galvan, F. del Valle, J. A. V. de la Mano and J. L. G. Fierro, *ChemSusChem*, 2009, **2**, 471–485.
53 T. Low, A. S. Rodin, A. Carvalho, Y. J. Jiang, H. Wang, F. N. Xia and A. H. C. Neto, *Phys. Rev. B: Condens. Matter Mater. Phys.*, 2014, **90**, 5.
54 Y. N. Zhang, J. N. Yun, K. Y. Wang, X. H. Chen, Z. Yang, Z. Y. Zhang, J. F. Yan and W. Zhao, *Comput. Mater. Sci.*, 2017, **136**, 12–19.
55 J. N. Hilfiker, M. Stadermann, J. N. Sun, T. Tiwald, J. S. Hale, P. E. Miller and C. Aracne-Ruddle, *Appl. Surf. Sci.*, 2017, **421**, 508–512.
56 S. Kattel, P. Atanassov and B. Kiefer, *Phys. Chem. Chem. Phys.*, 2013, **15**, 148–153.
57 J. Rossmeisl, Z. W. Qu, H. Zhu, G. J. Kroes and J. K. Norskov, *J. Electroanal. Chem.*, 2007, **607**, 83–89.
58 J. Rossmeisl, A. Logadottir and J. K. Norskov, *Chem. Phys.*, 2005, **319**, 178–184.
59 A. Valdes, Z. W. Qu, G. J. Kroes, J. Rossmeisl and J. K. Norskov, *J. Phys. Chem. C*, 2008, **112**, 9872–9879.

This journal is © The Royal Society of Chemistry 2020